

Fractional Spin Fluctuation as a Precursor of Quantum Spin Liquids: Majorana Dynamical Mean-Field Study for the Kitaev Model

Junki Yoshitake¹, Joji Nasu², and Yukitoshi Motome¹

¹*Department of Applied Physics, University of Tokyo, Bunkyo, Tokyo 113-8656, Japan*

²*Department of Physics, Tokyo Institute of Technology, Meguro, Tokyo 152-8551, Japan*

(Dated: September 2, 2016)

Experimental identification of quantum spin liquids remains a challenge, as the pristine nature is to be seen in asymptotically low temperatures. We here theoretically show that the precursor of quantum spin liquids appears in the spin dynamics in the paramagnetic state over a wide temperature range. Using the cluster dynamical mean-field theory and the continuous-time quantum Monte Carlo method, which are newly developed in the Majorana fermion representation, we calculate the dynamical spin structure factor, relaxation rate in nuclear magnetic resonance, and magnetic susceptibility for the honeycomb Kitaev model whose ground state is a canonical example of the quantum spin liquid. We find that dynamical spin correlations show peculiar temperature and frequency dependence even below the temperature where static correlations saturate. The results provide the experimentally-accessible symptoms of the fluctuating fractionalized spins evincing the quantum spin liquids.

PACS numbers: 71.10.Fd, 71.27.+a, 75.10.-b

The quantum spin liquid (QSL) has attracted much attention for decades, as a new state of matter in insulating magnets stabilized by quantum fluctuations [1]. Although several candidate materials have been studied, experimental identification of QSLs still remains a challenge in modern condensed matter physics [2, 3]. This is mainly because of the absence of conventional order parameters: it is hard to prove the lack of any symmetry breaking down to the lowest temperature (T). Many attempts were made also on the low- T behavior of thermodynamic quantities, for instance, the specific heat [4–6], which reflect the low-energy excitations specific to QSLs. All these efforts are nonetheless extremely difficult, as the asymptotically low- T physics might be sensitively affected by extrinsic factors, such as impurities and subordinate interactions.

On the other hand, QSLs are established in several theoretical models. Among them, the Kitaev model provides a canonical example of exact QSLs with fractional excitations in the ground state [7]. The model is believed to describe the anisotropic exchange interactions realized in insulating magnets with strong spin-orbit coupling, such as Ir oxides [8]. This has stimulated a new trend of exploration of QSLs in real materials [9–12]. Recently, several experimental efforts have been made on the identification of the fractional excitations in the paramagnetic state above the Néel temperature as a precursor to QSLs [13–16]. Indeed, such a signature in a wide T range was theoretically predicted for thermodynamic quantities [17]. However, the signature of fractionalization is most clearly visible in the dynamics, for which theoretical studies were limited to the ground state [18, 19]. Thus, the ‘missing link’ between theory and experiment exists in the dynamical properties in the experimentally-accessible T range. This is, however, a theoretical challenge as it requires to

handle both quantum and thermal fluctuations simultaneously.

In this Letter, we present numerical results on the dynamical properties of the Kitaev model at finite T . To take into account quantum and thermal fluctuations on an equal footing, we develop the cluster dynamical mean-field theory (CDMFT) and the continuous-time quantum Monte Carlo method (CTQMC) in the Majorana fermion representation of this quantum spin model. We calculate the experimentally measurable quantities: the dynamical spin structure factor, $S(\mathbf{q}, \omega)$, which is measured in the neutron scattering experiment, the relaxation rate in nuclear magnetic resonance (NMR), $1/T_1$, and the magnetic susceptibility χ , for both ferromagnetic (FM) and antiferromagnetic (AFM) cases. We show that the dynamical spin fluctuations in the paramagnetic state are strongly influenced by the thermal fractionalization of quantum spins. $S(\mathbf{q}, \omega)$ exhibits the growth of inelastic and quasi-elastic responses at very different T scales. Also, $1/T_1$ begins to increase below the temperature where the static spin correlations saturate, and shows a peak at very low T , despite the suppression of χ from the Curie-Weiss behavior. These unconventional features will provide a smoking gun for fractionalized spins in the Kitaev-type QSLs.

We consider the Kitaev model on a honeycomb lattice, whose Hamiltonian is given by [7]

$$\mathcal{H} = -J_x \sum_{\langle j,k \rangle_x} S_j^x S_k^x - J_y \sum_{\langle j,k \rangle_y} S_j^y S_k^y - J_z \sum_{\langle j,k \rangle_z} S_j^z S_k^z, \quad (1)$$

where S_j^p is the $p(=x, y, z)$ component of the $S = 1/2$ spin at site j . The sum of $\langle j, k \rangle_p$ is taken for the nearest-neighbor (NN) sites on three inequivalent bonds of the honeycomb lattice, as indicated in Fig. 1(a).

The exact solution for the ground state of the model (1) is obtained by introducing Majorana fermions [7]. A formulation, which is suitable for the following numerical calculations at finite T , is obtained by applying the Jordan-Wigner transformation to the one-dimensional chains composed of the J_x and J_y bonds and introducing two types of Majorana fermions c_j and \bar{c}_j [20–22]. Then, the Hamiltonian in Eq. (1) is rewritten as

$$\mathcal{H} = i \frac{J_x}{4} \sum_{(j,k)_x} c_j c_k - i \frac{J_y}{4} \sum_{(j,k)_y} c_j c_k - i \frac{J_z}{4} \sum_{(j,k)_z} \eta_r c_j c_k, \quad (2)$$

where $(j,k)_p$ is the NN pair satisfying $j < k$ on the p bond. Here, $\eta_r = i\bar{c}_j c_k$ is defined on each z bond (r is the bond index); η_r is a Z_2 variable taking ± 1 , as $\eta_r^2 = 1$ and it commutes with the Hamiltonian as well as all the other $\eta_{r'}$. The ground state is given by all $\eta_r = 1$, dictating a QSL with gapless or gapful excitations depending on the anisotropy in the coupling constants [7].

At finite T , however, the configuration of $\{\eta\}$ is disturbed by thermal fluctuations. Hence, the model in Eq. (2) describes itinerant Majorana fermions coupled to thermally-fluctuating classical variables η_r , which can be regarded as a variant of the double-exchange model. This allows one to utilize theoretical tools developed for fermion systems, such as the quantum Monte Carlo method [23]. In this study, we construct the CDMFT [24] for this Majorana fermion problem. By following the formulation for the double-exchange model [25] and using the path-integral representation for Majorana fermions [26], the effective action for a cluster embedded in a bath [see Fig. 1(a)] is given by

$$\mathcal{S}_{\text{eff}}^{\{\eta\}} = -T \sum_{j,k,n \geq 0} \chi_{j,-\omega_n} (\mathcal{G}_0(i\omega_n))_{j,k}^{-1} \chi_{k,\omega_n} + i \frac{J_z}{2} T \sum_{\langle j,k \rangle_{z,n}} \eta_r \chi_{j,-\omega_n} \chi_{k,\omega_n}, \quad (3)$$

where χ_{j,ω_n} is the Grassmann number corresponding to the Majorana operator c_j , and \mathcal{G}_0 represents the Weiss function including the effect of bath. For a given configuration of $\{\eta\}$, the impurity problem is exactly solvable and Green's function is obtained as $(G^{\{\eta\}}(i\omega_n))^{-1} = (\mathcal{G}_0(i\omega_n))^{-1} - h^{\{\eta\}}$, where $h^{\{\eta\}}$ is the matrix representation of the second term in Eq. (3). Local Green's function is also exactly calculated through $G(i\omega_n) = P(\{\eta\})G^{\{\eta\}}(i\omega_n)$, where $P(\{\eta\}) = Z^{\{\eta\}} / \sum_{\{\eta\}} Z^{\{\eta\}}$ with $Z^{\{\eta\}} = e^{-\mathcal{S}_{\text{eff}}^{\{\eta\}}} = \prod_{n \geq 0} \det[-G^{\{\eta\}}(i\omega_n)]$, as we can compute $G^{\{\eta\}}(i\omega_n)$ and $P(\{\eta\})$ for all $2^{N_c/2}$ configurations of $\{\eta\}$ in a N_c -site cluster [27]. The self-consistent equations in CDMFT are given as $\Sigma(i\omega_n) = (\mathcal{G}_0(i\omega_n))^{-1} - (G(i\omega_n))^{-1}$ and $(\mathcal{G}_0(i\omega_n))^{-1} = (\frac{1}{N} \sum_{\mathbf{k}} [i\omega_n - 2\mathcal{H}_0(\mathbf{k}) - \Sigma(i\omega_n)]^{-1})^{-1} + \Sigma(i\omega_n)$, where Σ is the self-energy, N is the number of

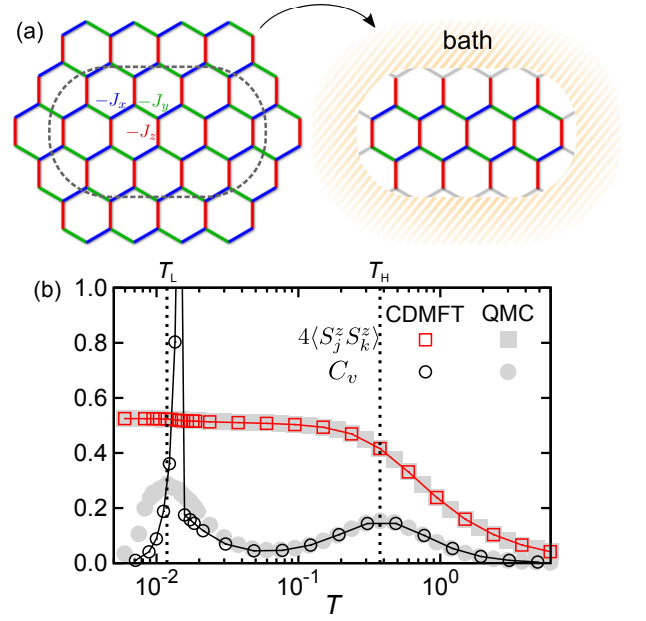


FIG. 1: (a) Schematic picture of the Kitaev model on the honeycomb lattice [Eq. (1)] and the mapping to a 26-sites cluster used in the Majorana CDMFT. (b) The specific heat C_v and equal-time spin correlations for NN sites, $\langle S_j^z S_k^z \rangle$, obtained by the Majorana CDMFT for the isotropic FM case. QMC data in Ref. [17] are plotted by gray symbols for comparison.

clusters in the whole lattice, and $\mathcal{H}_0(\mathbf{k})$ is the Fourier transform of the first and second terms in Eq. (2).

Thus, the Majorana CDMFT provides the *exact* results for thermodynamic quantities of the quantum spin model (1), except for the cluster approximation. This is a distinct advantage of the Majorana representation: the original quantum spin representation does not admit the exact enumeration. In addition, the cluster approximation works quite well in the current system with extremely short-range spin correlations [28], as demonstrated below. In the following calculations, we take the 26-sites cluster shown in Fig. 1(a), and consider 60×80 array of the unit cell [29]. Typically, the CDMFT loop is repeated for ten times until convergence.

A benchmark of the Majorana CDMFT is shown in Fig. 1(b). We compare the specific heat and the equal-time NN spin correlations $\langle S_j^p S_k^p \rangle$ obtained by CDMFT with those by QMC in Ref. [17]. The data are calculated for the isotropic FM case, $J_x = J_y = J_z = 1$ (the sign of $\langle S_j^p S_k^p \rangle$ is reversed for AFM). As indicated by two broad peaks in the specific heat in the QMC results, the system exhibits two crossovers at $T_H \sim 0.375$ and $T_L \sim 0.012$. The spin correlations grow down to $T \sim T_H$, while they saturate below T_H and do not show significant changes at T_L [17]. These behaviors are excellently reproduced by CDMFT, except for the low- T peak in the specific heat. The sharp anomaly in the CDMFT result at $T \simeq 0.014$ is

due to a phase transition by ordering of $\langle \eta \rangle$, which is an artifact of the mean-field nature of CDMFT. The comparison, however, shows that the CDMFT gives qualitatively correct results in a wide T range above the low- T crossover, i.e., $T \gtrsim 0.015$. We note that the quantum spin liquid state at sufficiently low T , where all $\eta_r = 1$, is also reproducible [29]. Thus, the present CDMFT enables to calculate the physical properties with sufficient precision in the wide T range except for the vicinity of T_L . In the following, we apply the CDMFT in this qualified T range above T_L to the study of spin dynamics, which one cannot compute by QMC.

In the calculations of dynamical quantities, we need an additional effort beyond the exact enumeration in the Majorana CDMFT. This is because the calculation of dynamical spin correlations $\langle S_j^p(\tau) S_k^p \rangle$ requires the imaginary time evolution of the \bar{c} variables that compose the conserved quantities η . To compute $\langle S_j^p(\tau) S_k^p \rangle$, we adopt the CTQMC based on the strong coupling expansion [30]. $\langle S_j^z(\tau) S_k^z \rangle$ on an r_0 bond is calculated as $\langle S_j^z(\tau) S_k^z \rangle = \sum_{\{\eta\}', \eta_{r_0} = \pm 1} P(\{\eta\}', \eta_{r_0}) \langle S_j^z(\tau) S_k^z \rangle^{\{\eta\}'}$ by using the CDMFT solutions; here, $\{\eta\}'$ represents the configurations of η_r except for the r_0 bond, and $\langle S_j^z(\tau) S_k^z \rangle^{\{\eta\}'}$ is calculated for a given $\{\eta\}'$ by CTQMC. As the interaction between Majorana fermions lies only on the r_0 bond, it is sufficient to solve the two-site impurity problem in CTQMC. In the CTQMC calculations, we typically run 10^7 steps with measurement at every 20 steps, after 10^5 steps of initial relaxation, for each $\langle S_j^p(\tau) S_k^p \rangle^{\{\eta\}'}$. $\langle S_j^p(\tau) S_k^p \rangle$ for $p = x, y$ are obtained by taking the lattice coordinate so that $p = z$. In the following, we present the results for the isotropic coupling, $J_x = J_y = J_z = J$, where the ground state is a gapless quantum spin liquid [7]. We compute both FM and AFM cases [32] with setting $|J| = 1$ as the energy unit. The systematic study of the anisotropic cases will be reported elsewhere.

Using the Majorana CDMFT+CTQMC, we calculate the dynamical spin structure factor, NMR relaxation rate, and magnetic susceptibility. The dynamical spin structure factor is defined as $S(\mathbf{q}, \omega) = 1/(3NN_c) \sum_p \sum_{j,k} e^{i\mathbf{q} \cdot (\mathbf{r}_j - \mathbf{r}_k)} S_{j,k}^p(\omega)$, where $S_{j,k}^p(\omega)$ is obtained by solving $\langle S_j^p(\tau) S_k^p \rangle = \int d\omega S_{j,k}^p(\omega) e^{-\omega\tau}$ by the maximum entropy method [31]. We confirmed the validity of the procedures by the fact that the low- T result with $\langle \eta \rangle \simeq 1$ (beyond the quantified T range) reproduces the $T = 0$ solution [18]. The NMR relaxation rate is obtained by using the relation, $1/T_1 \propto S_{j,k}^x(\omega = 0) + S_{j,k}^y(\omega = 0)$; we compute the contributions from onsite and NN-site correlations separately, as the hyperfine coupling is unknown. The magnetic susceptibility is calculated as $\chi^p = 1/(NN_c) \sum_{j,k} \int d\tau \langle S_j^p(\tau) S_k^p \rangle$; $\chi^x = \chi^y = \chi^z = \chi$ for the isotropic coupling.

Figure 2 shows the T dependences of the dynamical spin structure factor $S(\mathbf{q}, \omega)$ for both FM and AFM

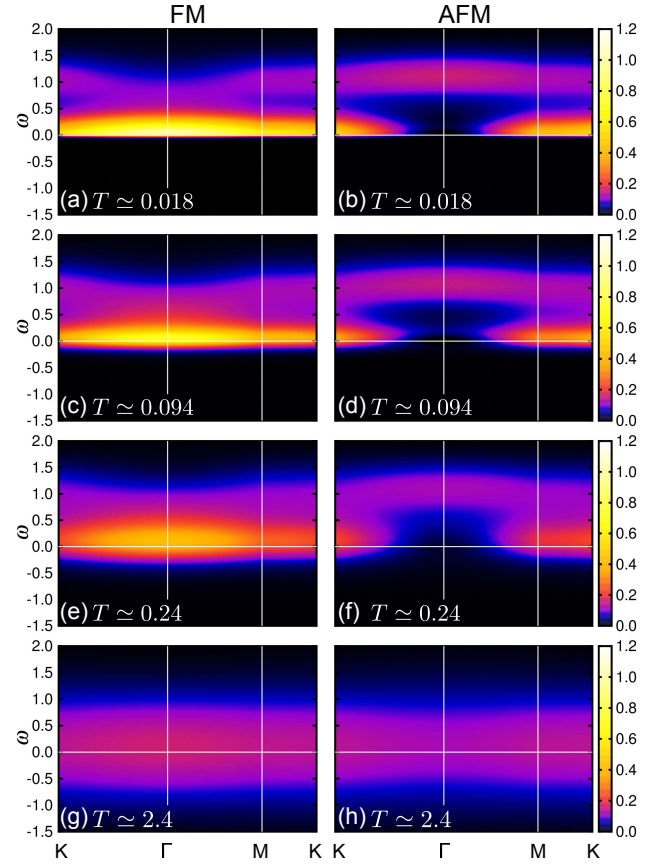


FIG. 2: The dynamical spin structure factor $S(\mathbf{q}, \omega)$ obtained by the Majorana CDMFT+CTQMC for the (a)(c)(e)(g) FM and (b)(d)(f)(h) AFM cases at (a)(b) $T \simeq 0.018$, (c)(d) $T \simeq 0.094$, (e)(f) $T \simeq 0.24$, and (g)(h) $T \simeq 2.4$.

cases. At high $T > T_H$, $S(\mathbf{q}, \omega)$ shows only a diffusive response at $\omega \sim 0$ with less \mathbf{q} dependence in both FM and AFM cases, as shown in Figs. 2(g) and 2(h). The \mathbf{q} - ω dependence begins to develop while lowering T below $T_H \sim 0.375$; the diffusive weight shifts to a positive ω region ranging to $\omega \sim J$ below T_H [Figs. 2(e) and 2(f)], and at the same time, the quasi-elastic component at $\omega \sim 0$ grows gradually [Figs. 2(c) and 2(d)]. The quasi-elastic response is large around the Γ point in the FM case, whereas it is distributed on the Brillouin zone boundary (along the K-M line) in the AFM case. With further decreasing T , the intensity of the quasi-elastic peak continues to increase while approaching $T_L \sim 0.012$, as shown in Figs. 2(a) and 2(b). The low- T behavior converges on the ground state solution, which has a sharp peak at $\omega \sim 0.12J$ together with an incoherent weight at $\omega \sim J$ [18].

To see these behaviors more clearly, we show the data at the Γ and K points, denoted as $S(\Gamma, \omega)$ and $S(K, \omega)$, respectively, in Fig. 3. Note that $S(K, \omega)$ is the same for the FM and AFM cases by symmetry. In the FM case, $S(\Gamma, \omega)$ and $S(K, \omega)$ show qualitatively similar T - ω

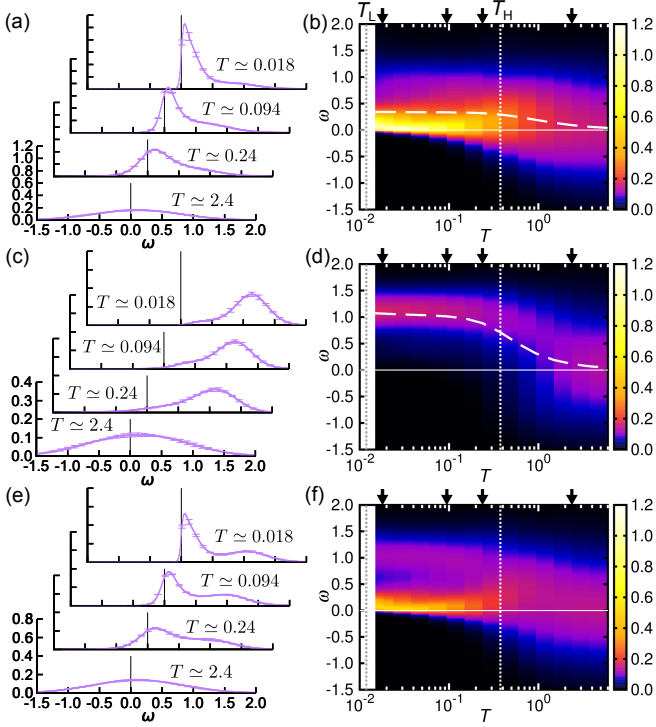


FIG. 3: $S(\Gamma, \omega)$ for the (a) FM and (c) AFM cases, and (e) $S(K, \omega)$ at several T . (e) is common to the FM and AFM cases. The corresponding contour plots in the T - ω plane are shown in (b)(d)(f). The arrows indicate the temperatures used for the data in (a)(c)(e). The dashed curves represent the average frequency of $S(\mathbf{q}, \omega)$ (see the text for details). In (a)(c)(e), the errorbars are shown for every ten data along the ω axis.

dependence, as shown in Figs. 3(a)(b) and 3(e)(f); the inelastic response at $\omega \sim J$ appears below T_H , and the quasi-elastic one at $\omega \sim 0$ rapidly grows as approaching T_L . On the other hand, in the AFM case, the strong quasi-elastic intensity at low T is absent, while the inelastic response at $\omega \sim J$ arises below T_H , as in the FM case, as shown in Figs. 3(c)(d).

Despite the different \mathbf{q} dependence reflecting the sign of J , $S(\mathbf{q}, \omega)$ exhibits common characteristic ω - T dependence: the emergence of the inelastic response at $\omega \sim J$ for $T \lesssim T_H$, and the rise of the quasi-elastic response as $T \rightarrow T_L$. These peculiar behaviors are regarded as the signatures of the fractionalization of quantum spins into two types of Majorana fermions, itinerant “matter fermions” and localized “fluxes”, which correspond to c and η in Eq. (2), respectively. The previous QMC studies revealed that the matter fermions and fluxes affect the thermodynamics at very different T scales [17, 23]; the kinetic energy of matter fermions, which is equivalent to the equal-time spin correlations $\langle S_j^p S_k^p \rangle$ [see Eqs. (1) and (2)], is gained at $T \sim T_H$, whereas the fluxes shows a condensation at $T \sim T_L$ to the flux-free state with all $\eta_r = 1$. Our results of $S(\mathbf{q}, \omega)$ obtained above indicate

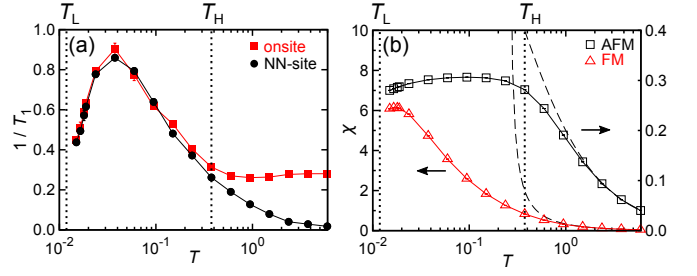


FIG. 4: T dependences of (a) the NMR relaxation rate $1/T_1$ and (b) the magnetic susceptibility χ . In (b), the dashed curves represent the Curie-Weiss behavior χ_{CW} .

that the former is closely related to the evolution of the inelastic response at $\omega \sim J$ below T_H , while the latter to the rise of the quasi-elastic response as approaching T_L .

The relation between the inelastic response and the matter fermions is grasped through two sum rules for the dynamical spin structure factor. For instance, at the Γ point, the sum rules read $\int S^p(\Gamma, \omega) d\omega = \langle S_j^p S_k^p \rangle + 1/4$ and $\int \omega S^z(\Gamma, \omega) d\omega = (J_x \langle S_j^x S_k^x \rangle + J_y \langle S_j^y S_k^y \rangle)/2$ (similarly for $p = x, y$), where $\langle S_j^p S_k^p \rangle$ denotes the equal-time NN spin correlation [33]. As mentioned above, in the Kitaev model, $\langle S_j^p S_k^p \rangle$ corresponds to the kinetic energy of the matter fermions. Hence, when we compute the average frequency of $S^p(\Gamma, \omega)$ by the ratio of the two sum rules, $\bar{\omega} \equiv \int \omega S^z(\Gamma, \omega) d\omega / \int S^z(\Gamma, \omega) d\omega$, the kinetic energy gain of the matter fermions at $T \sim T_H$ results in the shift of $\bar{\omega}$ from almost zero to a nonzero positive value. This is indeed seen in Figs. 3(b) and 3(d), where $\bar{\omega}$ is plotted by the dashed curves. The difference of the values of low- T $\bar{\omega}$ between the FM and AFM cases is also accounted for by the opposite sign of the NN contribution in the first sum rule.

On the other hand, below $T \sim T_L$, the quasi-elastic response converges on the sharp peak at $\omega \sim 0.12J$ with a flux gap $\Delta \simeq 0.065J$ [7] in the $T = 0$ solution [18]. As the fluxes are proliferated above $T \sim T_L$ [17], the decay of the quasi-elastic response for $T \gtrsim T_L$ is considered as a consequence of the thermally excited fluxes. Indeed, the flux gap is smeared out in our results above $T \sim T_L$.

We find that the influence of excited fluxes is more clearly visible in the NMR relaxation rate $1/T_1$. Figure 4(a) shows the CDMFT+CTQMC results of $1/T_1$: we plot the value of $S_{j,k}^x(\omega = 0) + S_{j,k}^y(\omega = 0)$ in the FM case (the NN component changes its sign in the AFM case). In the high- T region above T_H , as expected for the conventional paramagnets [34], the onsite component is nearly T independent, while the NN-site one increases gradually with decreasing T , reflecting the growth of equal-time spin correlations $\langle S_j^p S_k^p \rangle$ in Fig. 1(b). Below T_H , however, both components increase and show a peak at slightly above T_L , despite the saturation of equal-time correlations [35]. The pronounced peak is regarded as the consequence of thermally excited fluxes above T_L , as

the suppression of $1/T_1$ for $T \lesssim T_L$ is due to the formation of the flux gap in the low- T limit [18]. The unexpected behavior below T_H is also seen in comparison with the magnetic susceptibility χ in Fig. 4(b); despite the enhancement of $1/T_1$, χ is suppressed from the Curie-Weiss behavior, $\chi_{CW} = 1/(4T - J)$, which is obtained by the standard mean-field approximation in the original spin representation. These T dependences of $1/T_1$, χ , and $\langle S_j^p S_k^p \rangle$ below T_H are highly unusual; in conventional quantum magnets, the dynamical spin correlations grow with the static ones. The dichotomy between the static and dynamical correlations is a clear signature of fractionalization of quantum spins [29].

In summary, we have presented a comprehensive set of theoretical results for dynamical and static spin correlations, which evince fluctuating fractionalized spins in the Kitaev QSLs. The results are unveiled by using the Majorana CDMFT+CTQMC method developed in the current study. Experimentally, an unusual inelastic response, similar to our results of $S(\mathbf{q}, \omega)$, was observed in the recent neutron scattering experiment for a Kitaev candidate, α -RuCl₃ [16]. Also, a similar peak in $1/T_1$ to our results was observed for another candidate, Li₂RhO₃ [36]. The deviation of χ from χ_{CW} was already reported in many materials [9–11]. Obviously, further systematic studies for the Kitaev candidate materials are highly desired to test our predictions. Our results will stimulate the rapidly-evolving “pincer attack” by theory and experiment for the long standing issue—the identification of fractionalized spins in QSLs.

The authors thank M. Imada, Y. Kato, M. Udagawa, and Y. Yamaji for fruitful discussions. This research was supported by KAKENHI (No. 24340076 and 15K13533), the Strategic Programs for Innovative Research (SPIRE), MEXT, and the Computational Materials Science Initiative (CMSI), Japan.

—Supplemental Material—

Cluster size dependence

The CDMFT is an approximation which replaces the infinite-size system by a finite-size cluster embedded in a bath [see Fig. 1(a) in the main text]. It becomes exact when the cluster size is increased to infinity. Thus, it is crucial how the results converge to the thermodynamic limit as a function of the cluster size.

Figure S1 shows the cluster size dependence of the magnetic susceptibility obtained by the CDMFT+CTQMC method. The data are plotted as functions of the cluster width in the xy direction, not the total number of lattice sites included in the cluster. This is because the width in the xy direction is rather relevant compared to that in the z direction in the

present CDMFT, presumably due to the Majorana representation based on the Jordan-Wigner transformation along the xy chain. Other physical quantities calculated in the main text behave in a similar manner.

As shown in Fig. S1, for both FM and AFM cases, the results show good convergence when increasing the cluster size. In fact, the convergence is very quick, except for the low- T region in the vicinity of the artificial transition temperature $T_c \simeq 0.014$, which is close to $T_L \simeq 0.012$ [see Fig. 1(b) in the main text]. For instance, the data at $T \simeq 0.038$, which is sufficiently high compared to T_c , are almost unchanged while increasing the cluster width larger than ~ 4 in all the different series of the clusters. On the other hand, while lowering temperature and approaching T_c , the cluster size dependence becomes substantial, as shown in the data at $T \simeq 0.017$ in the figure. Nevertheless, the data for the 26-site cluster, which is used in the main text [the width is ~ 4.3 in the series of Fig. S2(a)], give sufficiently converged results: the remnant relative errors are $\lesssim 3\%$ for both FM and AFM cases. Note that the remnant errors become discernible only in the very vicinity of T_c . From these observations, we confirmed that our data in the wide range of T above $T_c \simeq 0.014$ are quantitatively correct and well reproduce the behaviors expected in the thermodynamic limit.

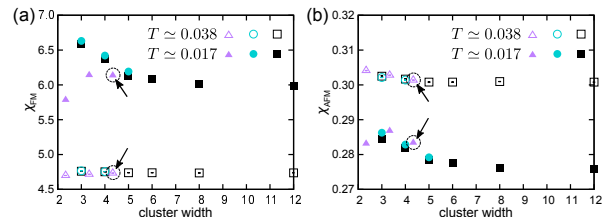


FIG. S1: Cluster size dependence of the magnetic susceptibility for (a) the FM and (b) AFM cases. The different symbols represent the different series of the clusters: triangles, circles, and squares correspond to Fig. S2(a), S2(b), and S2(c), respectively. The data in the dashed circles with arrows indicate the results for the 26-site cluster used in the calculations in the main text. The definition of the cluster width is described in the caption of Fig. S2.

CDMFT+CTQMC results for $T < T_L$

As mentioned in the main text, the CDMFT calculation exhibits a phase transition by ordering of $\langle \eta_r \rangle$ at $T \simeq 0.014$ because of the mean-field nature of CDMFT. Below the critical temperature, $\langle \eta_r \rangle$ becomes almost 1, namely, the state is almost similar to the flux-free ground state. In the ground state, $S(\mathbf{q}, \omega)$ shows a small gap $\simeq 0.065J$ due to the gapped flux excitation [18]. In Fig. S3, we show the CDMFT+CTQMC results for the dynamical spin structure factor at $T = 0.00825$, which is

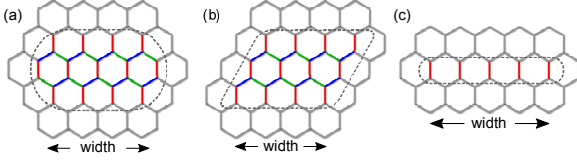


FIG. S2: Schematic picture of three series of the clusters used in Fig. S1. In each series of clusters, the cluster size is varied by the cluster width in the xy direction, while keeping the width in the z direction. The cluster width in the xy direction is given by the average number of the z -bonds (indicated by the red lines in the figures), which is used in the plots in Fig. S1. In these examples, the cluster width is (a) $13/3 \simeq 4.3$, (b) 4, and (c) 5.

well below the critical temperature as well as T_L . The result exhibits the flux gap, consistent with the previous results at $T = 0$. This further supports the validity of our CDMFT+CTQMC calculations. In Figs. 2 and 3 in the main text, the flux gap is smeared out and not clearly visible as the fluxes are excited by thermal fluctuations above T_L .

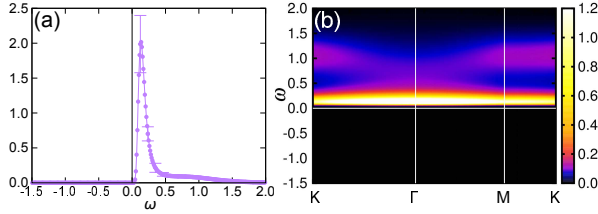


FIG. S3: (a) $S(\Gamma, \omega)$ and (b) $S(\mathbf{q}, \omega)$ at $T = 0.00825$ for the FM case. In (a), the errorbars are shown for every ten data along the ω axis.

Plots of Fig. 4 in the T -linear scale

In Fig. 4 in the main text, we show the NMR relaxation rate $1/T_1$ and the magnetic susceptibility χ as functions of $\ln T$. For reference, we present them in the T -linear scale in Fig. S4.

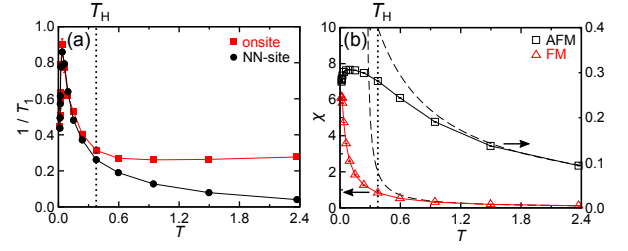


FIG. S4: The same plots as Fig. 4 in the main text in the T -linear scale.

- J.-H. Chung, D. G. Nocera, and Y. S. Lee, *Spin Dynamics of the Spin-1/2 Kagome Lattice Antiferromagnet $\text{ZnCu}_3(\text{OH})_6\text{Cl}_2$* , Phys. Rev. Lett. **98**, 107204 (2007).
- [5] Y. Okamoto, M. Nohara, H. Aruga-Katori, and H. Takagi, *Spin-Liquid State in the $S = 1/2$ Hyperkagome Antiferromagnet $\text{Na}_4\text{Ir}_3\text{O}_8$* , Phys. Rev. Lett. **99**, 137207 (2007).
- [6] S. Yamashita, Y. Nakazawa, M. Oguni, Y. Oshima, H. Nojiri, Y. Shimizu, K. Miyagawa, and K. Kanoda, *Thermodynamic properties of a spin-1/2 spin-liquid state in a κ -type organic salt*, Nature Phys. **4**, 459 (2008).
- [7] A. Kitaev, *Anyons in an exactly solved model and beyond*, Ann. Phys. **321**, 2 (2006).
- [8] G. Jackeli and G. Khaliullin, *Mott Insulators in the Strong Spin-Orbit Coupling Limit: From Heisenberg to a Quantum Compass and Kitaev Models*, Phys. Rev. Lett. **102**, 017205 (2009).
- [9] Y. Singh and P. Gegenwart, *Antiferromagnetic Mott insulating state in single crystals of the honeycomb lattice material Na_2IrO_3* , Phys. Rev. B **82**, 064412 (2010).
- [10] Y. Singh, S. Manni, J. Reuther, T. Berlijn, R. Thomale, W. Ku, S. Trebst, and P. Gegenwart, *Relevance of the Heisenberg-Kitaev Model for the Honeycomb Lattice Iridates A_2IrO_3* , Phys. Rev. Lett. **108**, 127203 (2012).
- [11] K. W. Plumb, J. P. Clancy, L. J. Sandilands, V. V. Shankar, Y. F. Hu, K. S. Burch, H.-Y. Kee, and Y.-J. Kim, *α - RuCl_3 : A spin-orbit assisted Mott insulator on a honeycomb lattice*, Phys. Rev. B **90**, 041112(R) (2014).
- [12] Y. Kubota, H. Tanaka, T. Ono, Y. Narumi, and K. Kindo, *Successive magnetic phase transitions in α - RuCl_3 : XY-like frustrated magnet on the honeycomb lattice*, Phys. Rev. B **91**, 094422 (2015).
- [13] H. Gretarsson, J. P. Clancy, Y. Singh, P. Gegenwart, J. P. Hill, J. Kim, M. H. Upton, A. H. Said, D. Casa, T. Gog, and Y.-J. Kim, *Magnetic excitation spectrum of Na_2IrO_3 probed with resonant inelastic x-ray scattering*, Phys. Rev. B **87**, 220407(R) (2013).
- [14] J. A. Sears, M. Songvilay, K. W. Plumb, J. P. Clancy, Y. Qiu, Y. Zhao, D. Parshall, and Y.-J. Kim, *Magnetic order in α - RuCl_3 : A honeycomb-lattice quantum magnet with strong spin-orbit coupling*, Phys. Rev. B **91**, 144420 (2015).
- [15] L. J. Sandilands, Y. Tian, K. W. Plumb, Y.-J. Kim, and K. S. Burch, *Scattering Continuum and Possible Fractionalized Excitations in α - RuCl_3* , Phys. Rev. Lett. **114**, 147201 (2015).
- [16] A. Banerjee, C. A. Bridges, J.-Q. Yan, A. A. Aczel, L. Li, M. B. Stone, G. E. Granroth, M. D. Lumsden, Y. Yiu, J. Knolle, D. L. Kovrizhin, S. Bhattacharjee, R. Moess-

- [1] P. W. Anderson, *Resonating valence bonds: a new kind of insulator*, Mater. Res. Bull. **8**, 153 (1973).
- [2] L. Balents, *Spin liquids in frustrated magnets*, Nature **464**, 199 (2010).
- [3] C. Lacroix, P. Mendels, and F. Mila, *Introduction to Frustrated Magnetism*, Springer Series in Solid-State Sciences (Springer, Heidelberg, 2011).
- [4] J. S. Helton, K. Matan, M. P. Shores, E. A. Nytko, B. M. Bartlett, Y. Yoshida, Y. Takano, A. Suslov, Y. Qiu,

- ner, D. A. Tennant, D. G. Mandrus, S. E. Nagler, *Proximate Kitaev quantum spin liquid behaviour in a honeycomb magnet*, Nature Materials, nmat4604 (2016).
- [17] J. Nasu, M. Udagawa, and Y. Motome, *Thermal fractionalization of quantum spins in a Kitaev model: Temperature-linear specific heat and coherent transport of Majorana fermions*, Phys. Rev. B **92**, 115122 (2015).
- [18] J. Knolle, D. L. Kovrizhin, J. T. Chalker, and R. Moessner, *Dynamics of a Two-Dimensional Quantum Spin Liquid: Signatures of Emergent Majorana Fermions and Fluxes*, Phys. Rev. Lett. **112**, 207203 (2014).
- [19] J. Knolle, G.-W. Chern, D. L. Kovrizhin, R. Moessner, and N. B. Perkins, *Raman Scattering Signatures of Kitaev Spin Liquids in $A_2\text{IrO}_3$ Iridates with $A=\text{Na}$ or Li* , Phys. Rev. Lett. **113**, 187201 (2014).
- [20] H.-D. Chen and J. Hu, *Exact mapping between classical and topological orders in two-dimensional spin systems*, Phys. Rev. B **76**, 193101 (2007).
- [21] X.-Y. Feng, G.-M. Zhang, and T. Xiang, *Topological Characterization of Quantum Phase Transitions in a Spin-1/2 Model*, Phys. Rev. Lett. **98**, 087204 (2007).
- [22] H.-D. Chen, and Z. Nussinov, *Exact results of the Kitaev model on a hexagonal lattice: spin states, string and brane correlators, and anyonic excitations*, J. Phys. A Math. Theor. **41**, 075001 (2008).
- [23] J. Nasu, M. Udagawa, and Y. Motome, *Vaporization of Kitaev Spin Liquids*, Phys. Rev. Lett. **113**, 197205 (2014).
- [24] G. Kotliar, S. Y. Savrasov, G. Pálsson, and G. Biroli, *Cellular Dynamical Mean Field Approach to Strongly Correlated Systems*, Phys. Rev. Lett. **87**, 186401 (2001).
- [25] N. Furukawa, *Transport Properties of the Kondo Lattice Model in the Limit $S = \infty$ and $D = \infty$* , J. Phys. Soc. Jpn. **63**, 3214 (1994).
- [26] J. Nilsson and M. Bazzanella, *Majorana fermion description of the Kondo lattice: Variational and path integral approach*, Phys. Rev. B **88**, 045112 (2013).
- [27] M. Udagawa, H. Ishizuka, and Y. Motome, *Non-Kondo Mechanism for Resistivity Minimum in Spin Ice Conduction Systems*, Phys. Rev. Lett. **108**, 066406 (2012).
- [28] G. Baskaran, S. Mandal, and R. Shankar, *Exact Results for Spin Dynamics and Fractionalization in the Kitaev Model*, Phys. Rev. Lett. **98**, 247201 (2007).
- [29] See Supplemental Material.
- [30] P. Werner, A. Comanac, L. de' Medici, M. Troyer, and A. J. Mills, *Continuous-Time Solver for Quantum Impurity Models*, Phys. Rev. Lett. **97**, 076405 (2006).
- [31] M. Jarrell and J. E. Gubernatis, *Bayesian inference and the analytic continuation of imaginary-time quantum Monte Carlo data*, Phys. Rep. **269**, 133 (1996).
- [32] We note that $S(\mathbf{q}, \omega)_{\text{AFM}} = -S(\mathbf{q}, \omega)_{\text{FM}} + 2S(\mathbf{q} = \mathbf{K}, \omega)$, where $S(\mathbf{q} = \mathbf{K}, \omega) = S_{j,j}^p(\omega)$ is common to the FM and AFM cases.
- [33] P. C. Hohenberg and W. F. Brinkman, *Sum rules for the frequency spectrum of linear magnetic chains*, Phys. Rev. B **10**, 128 (1973).
- [34] T. Moriya, *Nuclear Magnetic Relaxation in Antiferromagnetics, II*, Prog. Theor. Phys., **16**, 641 (1956).
- [35] The difference between the two components corresponds to $S(\Gamma, \omega = 0)$ in the AFM case [see Fig. 3(d)]. It becomes small after the growth of spin correlations below T_H , as it is proportional to the probability of aligning two spins on a z bond parallel to the z direction without an energy cost.
- [36] P. Khuntia, S. Manni, F. R. Foronda, T. Lancaster, S. J. Blundell, P. Gegenwart, and M. Baenitz, *Local Magnetism and Spin Dynamics of the Frustrated Honeycomb Rhodate Li_2RhO_3* , preprint (arXiv:1512.04904).